Article

Thin Film Fabrication by Pulsed Laser Deposition from TiO$_2$ Targets in O$_2$, N$_2$, He, or Ar for Dye-Sensitized Solar Cells

Dorel F. Albu [1], Jeanina Lungu [2], Gianina Popescu-Pelin [3], Cristian N. Mihăilescu [3,*], Gabriel Socol [3], Adrian Georgescu [2], Marcela Socol [4], Alexandra Bănică [3], Victor Ciupina [1,2] and Ion N. Mihailescu [3]

[1] Faculty of Physics, University of Bucharest, 077125 Magurele, Romania; dorel.albu@cne.ro (D.F.A.); vciupina@univ-ovidius.ro (V.C.)
[2] Department of Physics, Ovidius University of Constanta, 900527 Constanta, Romania; jmatei@univ-ovidius.ro (J.L.); contact.adriangeorgescu@gmail.com (A.G.)
[3] Lasers Department, National Institute for Lasers, Plasma and Radiation Physics, 077125 Magurele, Romania; gianina.popescu@inflpr.ro (G.P.-P.); gabriel.socol@inflpr.ro (G.S.); alexandra.banica@inflpr.ro (A.B.); ion.mihailescu@inflpr.ro (I.N.M.)
[4] Laboratory of Optical Processes in Nanostructured Materials, National Institute of Materials Physics, 077125 Magurele, Romania; marcela.socol@infim.ro
[*] Correspondence: cristi.mihailescu@inflpr.ro

Abstract: Active semiconductor layers of TiO$_2$ were synthesized via pulsed laser deposition in He, N$_2$, O$_2$, or Ar to manufacture DSSC structures. As-prepared nanostructured TiO$_2$ coatings grown on FTO were photosensitized by the natural absorption of the N719 (Ruthenium 535-bis TBA) dye to fabricate photovoltaic structures. TiO$_2$ photoanode nanostructures with increased adsorption areas of the photosensitizer (a combination with voluminous media) were grown under different deposition conditions. Systematic SEM, AFM, and XRD investigations were carried out to study the morphological and structural characteristics of the TiO$_2$ nanostructures. It was shown that the gas nature acts as a key parameter of the architecture and the overall performance of the deposited films. The best electro-optical performance was reached for photovoltaic structures based on TiO$_2$ coatings grown in He, as was demonstrated by the short-circuit current (*Isc*) of 5.40 mA, which corresponds to the higher recorded roughness (of 44 ± 2.9 nm RMS). The higher roughness is thus reflected in a more efficient and deeper penetration of the dye inside the nanostructured TiO$_2$ coatings. The photovoltaic conversion efficiency (η) was 1.18 and 2.32% for the DSSCs when the TiO$_2$ coatings were deposited in O$_2$ and He, respectively. The results point to a direct correlation between the electro-optical performance of the prepared PV cells, the morphology of the TiO$_2$ deposited layers, and the crystallinity features, respectively.

Keywords: dye-sensitized solar cells; PLD; TiO$_2$; photovoltaic conversion efficiency; SEM; XRD; AFM

1. Introduction

The interest in sustainable energy technologies, especially in photovoltaics, which convert the solar radiation directly into electricity, have undergone tremendous development lately [1] as a consequence of the increased energy consumed worldwide [2,3].

The first conversion of solar radiation to electric energy by the use of a p-n-junction-type solar cell, in 1954, reached an efficiency of 6% only [4]. Dye-sensitized nanocrystalline TiO$_2$ solar cells (DSSCs), which are based on the mechanism of a fast regenerative photoelectrochemical process, were first reported in 1991 by Gratzel et al. [5].

TiO$_2$ is recognized as a promising electrode material for DSSCs because of the wide band gaps, which are suitable for interfacial electron transport [6–8]. In comparison to the conventional cells, the functional element, which is responsible for the light absorption (the dye), is separated in DSSCs from the charge carrier transport route. This makes it possible to use low-to-medium purity materials via a low-cost process, based on the realistic

energy-conversion efficiency, while the materials used in DSSCs are environmentally friendly [9]. Furthermore, the understanding of photoexcited electron kinetics in the photo-electrochemical cell throughout its functioning is crucial for the development of high-efficiency DSSCs [10,11].

The main components of DSSCs in a photoconversion device are the working electrode, the photoanode, the dye, the electrolyte, the catalyst, and the counter electrode. The photoanode stands as a key element in the DSSC cell configuration because it intermediates the absorption of smaller or larger amounts of the dye, which is in fact responsible for the light absorption. A large quantity of dye ensures a better absorption and the overall improvement of the cell conversion efficiency. Different photoanode materials have been tested to date. Among them, ZnO [12–15] and TiO_2 [16–19] are widely recognized and investigated [20,21]. Although ZnO possesses better carrier mobility than TiO_2, the instability in the acidic environment and the development of the dye aggregates present significant disadvantages. In addition, the electron injection in ZnO is slower than in TiO_2, which results in a low photocurrent [22,23].

The development of the photoanodes can efficiently harvest the light stands for the main focus in the field of DSSCs. It should be noted that the DSSCs with TiO_2-nanoparticle structures and Ruthenium-based dye achieved an overall efficiency of over 12% so far (lab scale) [7]. Nevertheless, the theoretical predicted maximum efficiency of DSSCs is, in this case, 32% [8]. The parameters to engineer a higher conversion efficiency are the increased dye pickup, the reduced recombination reaction, and the improved charge transport ability. The synthesis method, which is used for the efficient preparation of TiO_2 coatings, has an impact on the conversion efficiency of DSSCs [24,25]. In this respect, the pulsed laser deposition (PLD) technique is demonstrated to be a prospective approach for depositing homogeneous TiO_2 coatings. PLD is a versatile technique with multiple advantages, such as a superior deposition rate, film growth, surface roughness, and even the ability to control the nanoparticle size. The fine tuning of the deposition parameters, such as the energy, temperature, ambient pressure, and target-to-substrate separation distance is affordable in view of the fabrication process optimization [24,26,27]. According to text books on PLD [28,29], the process is a cumulative step-by-step procedure. One should therefore expect a linear increase in the film thickness with the applied number of pulses. It was also shown that the deposition rate depends on the nature and the pressure of the ambient gas. The larger the gas atoms/molecules, and the higher their pressure, and the smaller the thickness of the deposited layer because of the collisions between the ablated material and the ambient gas [28,29].

This study was devoted to the identification of the best deposition regime of thin layers for these particular applications. With this contribution, we focus on a new manufacturing method that is dedicated to the shaping and architecture of TiO_2 photoanodes in order to improve the performance of DSSCs for superior solar-cell fabrication and characterization. Thus, pulsed laser deposition was employed to synthesize the active TiO_2 thin films. The proposed photoanode structure is a TiO_2 bilayer that consists of a thin compact (buffer) layer and a thick nanostructured layer. The aim of the buffer layer, which is known also as a "blocking layer", is to shield the electrodes from the dye solution impact and the oxidation at high temperatures, which secures good mechanical contact [26]. Thus, PLD, a particularly appealing technique because of its capability to generate nanostructured films with customized features [30], was chosen to synthesize the active TiO_2 thin films.

2. Materials and Methods

2.1. Synthesis of PLD Bilayers

PLD experiments were carried out in a stainless-steel enclosure using an excimer laser source, COMPex Pro205, from Coherent (Göttingen, Germany), which operated with a KrF* active mixture, and generated pulses of $\lambda = 248$ nm, $\tau_{(FWHM)} \leq 25$ ns. The laser beam incidence angle onto the target surface was of $\sim$45°, while the target-to-substrate separation distance was 5 cm (a scheme of the experimental setup is available from [31,32]).

The PLD targets were prepared by the uniaxial pressing of appropriate amounts of TiO_2 (Sigma Aldrich—Saint Quentin Fallavier, France, 99.5% purity) powder at 6 MPa by using a pellet die with a 20-mm diameter. The pellets were further sintered at 700 °C in air for 12 h in an oven model (Carbolite CWF1100, Hope, UK). During the multipulse laser irradiation, the targets (pellets) were rotated at 50 rot/min to avoid piercing and to ensure a uniform deposition.

Commercial low-iron 2.2-mm-thick glass fluorine-doped tin oxide (SnO_2:F) (FTO) (7 ohm/square from Solaronix, Aubonne, Switzerland), double-side-polished Si (100), and ordinary glass slides were used as the deposition substrates for each deposition batch.

The laser fluence and the laser repetition rate were set at 2.8 J/cm^2 and 40 Hz, respectively. During the deposition, the substrate temperature was kept constant at 450 °C using a PID-Excel temperature controller. The coatings were grown in gases (oxygen, nitrogen, argon, or helium) of different dynamic pressures, and were then denoted as: $TiO_2\_O_2$; $TiO_2\_N_2$; TiO_2_Ar; and TiO_2_He, respectively. Each sample was obtained by the PLD of two TiO_2 layers. The first was a dense TiO_2 thin film deposited by 1000 subsequent laser pulses [26], while the second one was a thick nanostructured layer that was synthesized by applying different numbers of pulses, depending on the gas environment (Table 1). The presence of reactive (O_2 and N_2) versus inert (Ar and He) ambient gases during PLD is expected to influence the gas-phase reactions and the plume composition (generation of new species) [33,34]. Physical processes, such as the diffusion, deceleration, recombination, thermalization of the ablated species, attenuation, shock wave evolution, and clustering, are involved in the process [35].

All of the coatings were submitted to a postdeposition thermal treatment at 450 °C for 12 h in air. This is mandatory for the removal of the organic contamination, the facilitation of the electrical connection between the nanoparticles [36], and especially for the preservation of the prevalent content of the TiO_2 anatase phase.

Table 1. PLD deposition conditions of TiO_2 coatings.

Sample	Pressure (Pa)	Nature of the Gas	No. of Pulses
$TiO_2\_O_2$	10/100	Oxygen, O_2	1000/20,000
$TiO_2\_N_2$	10/100	Nitrogen, N_2	1000/80,000
TiO_2_Ar	8/80	Argon, Ar	1000/20,000
TiO_2_He	5.9/5900	Helium, He	1000/40,000

2.2. Solar Cell Fabrication

A schematic design of a solar cell is displayed in Figure 1. The thick nanostructured TiO_2 coatings grown on the FTO/glass covered with dense TiO_2 (Figure 1) were photosensitized with N719 (Ruthenium 535-bisTBA) dye, and cis-diisothiocyanato-bis(2,20-bipyridyl-4,40-carboxylato) ruthenium (II) bis(tetrabutylammonium) [37] (Solaronix, Aubonne, Switzerland), at 0.2 mM in absolute ethanol, by soaking at 80 °C for 2 h. The plate was next rinsed with absolute ethanol to remove the excess dye and was dried at 80 °C for 10 min [5]. Our preference for this dye is based on the general appreciation that this is the most optimized, friendly with medium and easy available on the market, with respect to all the other equivalences from the same or similar classes [9].

The platinum counter electrodes were prepared by spreading a few drops of 5 mM of $H_2[PtCl_6]\cdot 6H_2O$ solution in 2-propanol onto the conductive glass, followed by drying at 100 °C for 10 min, and then at 400 °C for 30 min.

The electrolyte liquid (Iodolyte TG-50, Solaronix, Aubonne, Switzerland) was drawn into the space between the electrodes by the capillary action. To assemble the DSSCs, the plates were secured with small bulldog clips [38,39].
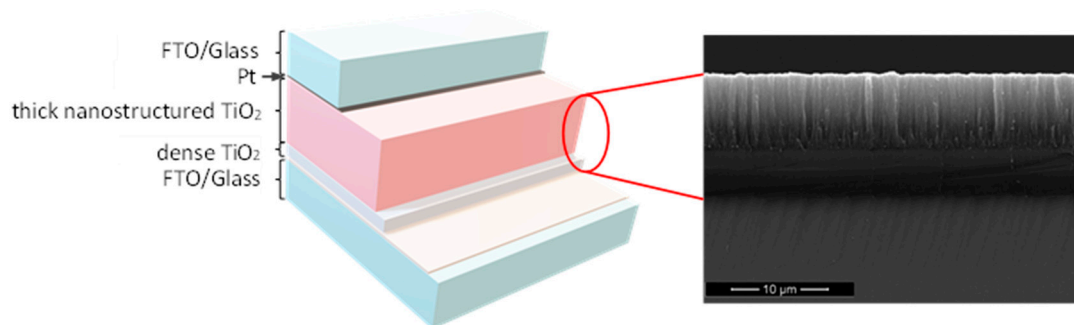
Figure 1. Schematic design of the solar cell (**left**); and cross-section SEM image of the TiO$_2$ coating (**right**).

2.3. Physicochemical Characterization

The thick nanostructured TiO$_2$ film morphologies were investigated by scanning electron microscopy (SEM) using an Apreo S microscope from Thermo Fisher Scientific, which was operated at a 10-kV acceleration voltage and 6.3 pA. In order to monitor the thicknesses of the active deposited coatings, the samples were examined in cross-section mode. Before observation, the samples were coated with a thin Au film ($\sim$12 nm) to prevent electrical charging.

The topologies (roughness) of the TiO$_2$ coatings were evaluated by atomic force microscopy (AFM) using the MultiView 4000 Nanonics system. The scan was performed in tapping mode and the investigated area was of (5×5) μm^2.

The crystalline phase identification was achieved by X-Ray diffraction (XRD) with an X'Pert Pro MPD diffractometer from Panalytical using Cu Kα radiation (λ = 1.5406 Å), which was set to work in Bragg–Brentano geometry with 2θ = (20–80)°, with an acquisition time of 2 s per step, and a 0.02° step size.

The electro-optic parameters of the DSSCs, i.e., the fill factor (*FF*), the photovoltaic conversion efficiency (η), the short-circuit current (I_{SC}), and the open-circuit voltage (V_{OC}) of the photovoltaic cells were measured under AM 1.5G standard irradiation conditions (1000 W/m^2) at 25 °C, using a Class A small-area solar simulator [40]. The cell surface was exposed to light through a circular slit of a 10-mm diameter, which resulted in an illumination area of about 0.785 cm^2. The current and voltage values were measured using two digital bench multimeters (*Mastech MS8050*) and a precision decade resistance box. The measurements were carried out at $\sim$45 s intervals in order to allow time for each reading to stabilize.

3. Results and Discussion

As is known from [41,42], the photovoltaic performance of the DSSCs is connected to the phase composition and the surface features of the TiO$_2$ nanoparticles. Moreover, the amount of dye absorbed by the photoanode can be monitored by the size and surface potential of the particles.

On the other hand, the total number of photogenerated carriers are related to the amount of dye absorbed, and they control the photovoltaic characteristics of the DSSC [41]. Next follows the corresponding results of our studies on the morphologies/topologies, compositions/structures, and overall performances of the deposited films.

3.1. Thin-Film Morphology and Topology

3.1.1. Top and Cross-Section SEM

Top-view and cross-section SEM micrographs of the TiO$_2$ coatings deposited under various environments (O$_2$, N$_2$, Ar, and He) are displayed in Figure 2. Specific morphological and topological features can be observed, depending on the pressure and nature of the background atmosphere.
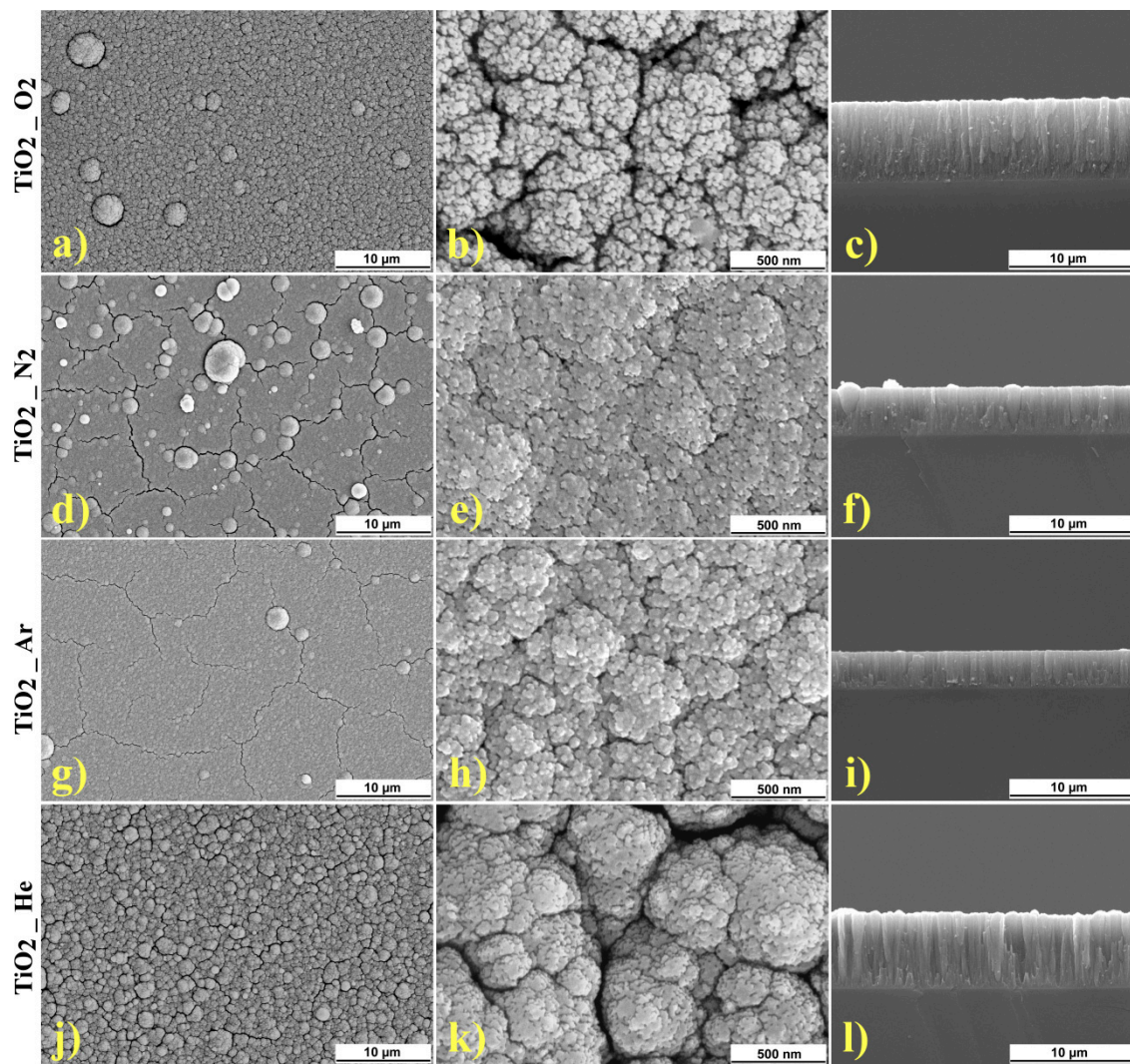
Figure 2. Typical top-view images of (**a**,**d**,**g**,**j**) low magnification, and (**b**,**e**,**h**,**k**) high-magnification, and (**c**,**f**,**i**,**l**) cross-section SEM micrographs of the thick nanostructured films deposited under various atmospheres (O_2, N_2, Ar, or He).

At a small magnification (5000×) (Figure 2a,d,g,j), the SEM micrographs of $TiO_2\_O_2$ and TiO_2_He reveal granular morphologies, with continuous and uniform appearances, similar to cauliflower inflorescence [43]. The presence of spherical particulates, with diameters ranging from a few tens of nm to several (up to 5) µm, is visible on all the deposited films. In the case of the $TiO_2\_N_2$ and TiO_2_Ar coatings, superficial cracks can be observed (Figure 2d,g), while for the N_2 ambient gas, the films contain an increased number of particulates (Figure 2d).

The advent of such particulates can be the result of one or several of the following mechanisms: (i) The explosive dislocation of the target surface material; (ii) The coalescence, or clustering, of the material in the plasma; (iii) The liquid-phase expulsion under the recoil pressure of the ablated substance; (iv) The blast-wave explosion at the melt–solid interface; and (v) Hydrodynamic instabilities on the target surface [32,44]. These mechanisms are characteristic to the incident laser wavelengths and fluence, the deposition geometry, and the gas nature and the pressure [45]. They require, in most cases, the presence of the liquid (melted) phase. The particulates could be present on either of the film surfaces, or embedded in the structure, and they could modify the local morphologies of the deposited films.

One should note that, the presence of particulates of any sort should absolutely be avoided in the case of deposited film utilization in optics, communications, and related

fields, but should be encouraged and promoted for use in biomedical, sensing, and chemical (catalytic) applications.

The particulate formation can be either promoted or inhibited and, thus, it is controlled via different approaches, such as: (i) The proper choice of laser wavelength and fluence; (ii) The application of external electric and/or magnetic fields; and/or (iii) The interception and elimination of the particulates by a second laser beam that is parallel to the surface [32].

High magnification SEM images—100,000× (Figure 2b,e,h,k)—show a uniform distribution of the small (nano) grains, with dimensions within the range of 15–45 nm. All of the samples display granular morphologies, with well-defined boundaries.

The batches are more compact in the cases of $TiO_2\_N_2$ and TiO_2_Ar (Figure 1e,h), as compared to $TiO_2\_O_2$ and TiO_2_He (Figure 2b,k). This is the probably related to the porosity degree, which is significantly lower in the first case.

A columnar growth of the deposited material, in all cases, can be noticed from the cross-section micrographs (Figure 2c,f,i,l). The thicknesses and the deposition rate values estimated from the cross-section images are collected in Table 2. The film thicknesses and deposition rates drastically change with the pressure, and especially with the nature of the background gas, mainly because of the collisions of the ablated species with the molecules or atoms of the surrounding gas. That is why the film deposited in Ar was the thinnest, at the limit of detection.

Table 2. Thicknesses, deposition rates, crystallinities by Scherrer equation, and roughness of TiO_2 thick nanostructured films grown under different gas atmospheres.

Sample Code	Thickness (µm)	Deposition Rate (Å/Pulse)	Average Crystallite Size (nm)	RMS (nm)
$TiO_2\_O_2$	6.49 ± 0.25	3.1 ± 0.1	9.9 ± 2.4	32.3 ± 4
$TiO_2\_N_2$	4 ± 0.48	0.5 ± 0.06	12.3 ± 3.4	30.3 ± 5.8
TiO_2_Ar	3 ± 0.25	1.4 ± 0.1	10.6 ± 2.7	40 ± 6.7
TiO_2_He	6.55 ± 0.53	1.6 ± 0.1	12.5 ± 3.8	44 ± 2.9

3.1.2. AFM

The topologies of the TiO_2 coatings, which were deposited under different gas atmospheres (O_2, N_2, Ar, and He), were further investigated by AFM, and typical 2D micrographs are shown in Figure 3.

The topological investigations confirmed the columnar growth of the coatings (3D micrographs—data not shown) and the uniform distribution of the material over the scanned area (5×5 µm^2), as is indicated by the SEM results. The estimated roughness (RMS) is given in Table 2.

It should be mentioned that the surface roughness essentially influences the energy coupling (absorption) with the incident light. It was thus shown that the laser absorption (of 1064 and 532 nm) increases with the surface roughness in the case of metals (Al, Cu, Au, Rh, Ti) [46]. This is a general behavior that is also verified in the cases of oxides, semiconductors, and other solid materials [47–49]. In particular, in the case of TiO_2, the highest roughness was observed for anatase, which resulted in higher light-energy absorption. In our case, the highest roughness was recorded for the films obtained in He, while the lowest roughness corresponds to the $TiO_2\_N_2$ depositions.
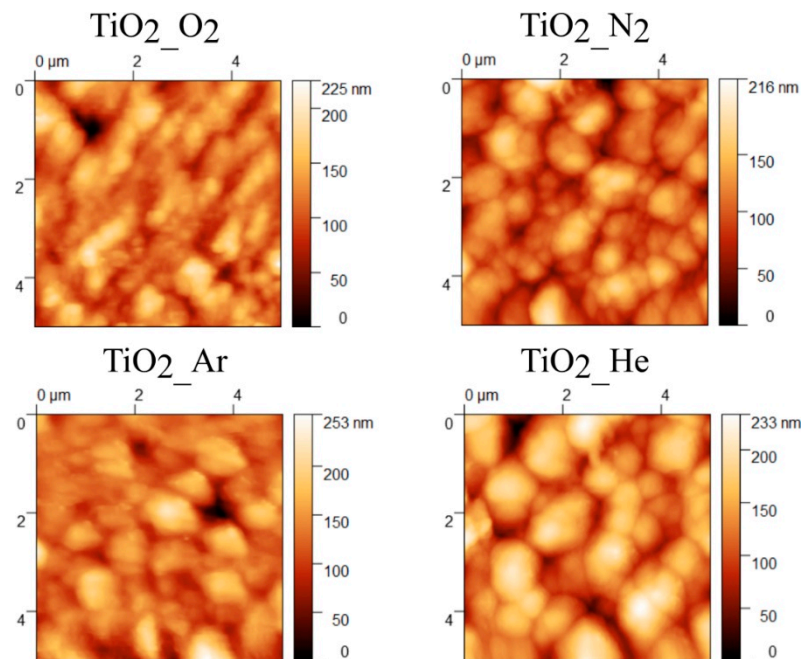
Figure 3. Typical AFM micrographs (5 × 5 μm² investigation area) of the coatings deposited by PLD under different gas environments (O_2, N_2, Ar, and He).

3.2. Thin-Film Structure and Composition

The crystalline structure of the coatings was next assessed by XRD, and the corresponding diffraction patterns are presented in Figure 4. One can note that the coatings essentially consist of an anatase and rutile phase mixture (anatase: pdf no. 00-021-1272; and rutile: pdf no. 00-021-1276), both of them with tetragonal structures and traces of orthorhombic brookite (pdf no. 01-075-2549).

The average crystallite size was calculated using the Scherrer equation (1), and the corresponding values are also given in Table 2:

$$D = \frac{k\lambda}{\beta \cos \theta}. \tag{1}$$

Here, D is the average crystallite size, $k = 0.9$ (Scherrer constant); λ is the wavelength of the X-ray source (0.15406 nm); β is the full width at half maximum (FWHM) value; and θ stands for the diffraction Bragg angle.

The main peak at 25.3°, which is assigned to the anatase plane (101), is clearly visible from the XRD diffractograms for all four batches of samples, which points to the prevalence of the anatase phase in the deposited mixture. The ration between the anatase versus the rutile contents is reflected in the roughness degree of the TiO_2 sample (layer) [50,51]. The peaks at 37.9° (400), 48.1° (200), 68.9° (116), and 75.2° (215) belong to the TiO_2 anatase, while those at 27.5° (110), 36.1° (101), 41.3° (111), 54.4° (211), 56.6° (220), and 62.8° (002) belong to the TiO_2 rutile phase. There are also some small diffraction peaks at the 30.9° (211), 33.1° (020), and 40.2° (202) planes that are associated with the TiO_2 brookite phase.

The XRD patterns reveal an increased crystallinity in the case of the TiO_2_He sample, and a low crystallinity for TiO_2_Ar, which is indicative of incomplete crystallization [52]. The absence of some diffraction maxima (37.9°, 62.8°, 68.9°, and 75.2°) is noticed for the TiO_2_Ar coating.

There is one observed, but very small, shift in the diffraction peaks in the recorded diffractograms, with respect to the TiO_2 PDF cards. These point to the strain that exists in the grown structures of the coatings [53].

The relatively broad X-ray diffraction peaks could indicate that the PLD coatings are composed of small nanoparticles [54]. This assertion is in good accordance with the

average crystallite size values of the TiO_2 films in Table 2, and with the observations by SEM and AFM.
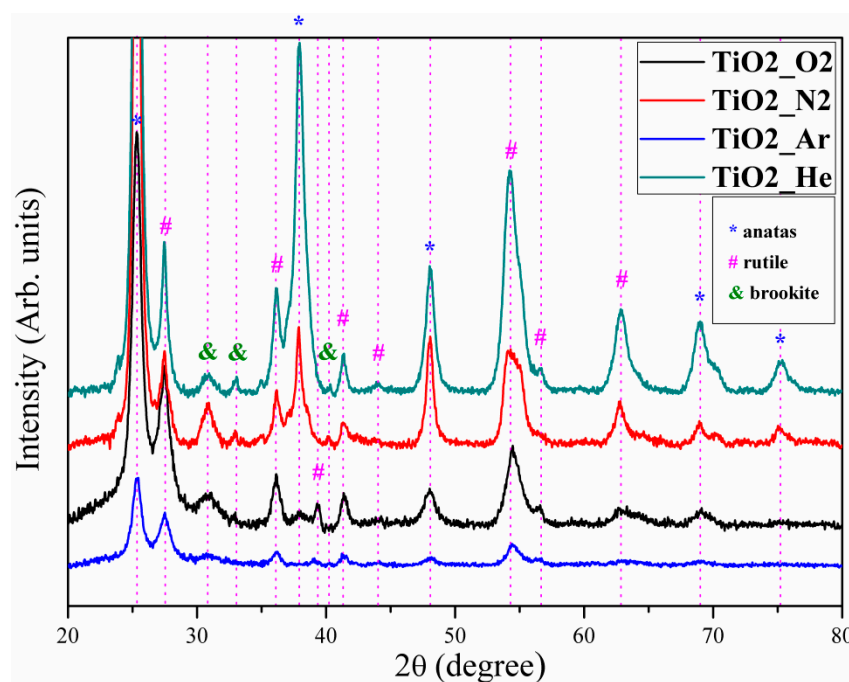

Figure 4. XRD patterns of TiO_2 coatings deposited by PLD in different ambient gases (O_2, N_2, Ar, or He).

3.3. PV Characteristics of Prepared Solar Cells

The typical values resulting from the electro-optical measurements performed on the DSSCs that were fabricated using photoelectrodes with PLD TiO_2 layers are displayed in Table 2 and are illustrated by the I–V curves in Figure 5. To determine the PV characteristics, 24 samples were prepared and analyzed (i.e., 6 for each gas atmosphere), and the acquired results were statistically interpreted.

An essential correlation can be noted between the identical hierarchy of the short-circuit current (Isc) and the photovoltaic conversion efficiency (η) values in Table 3, versus the roughness (RMS) in Table 2. Indeed, the highest Isc and η values were obtained for the TiO_2_He samples, which are characterized by the largest roughness among the deposited samples (44 ± 2.9 nm RMS). These are followed by the TiO_2_Ar, TiO_2_O$_2$, and TiO_2_N$_2$ samples, precisely in the order of their roughness of 40 ± 6.7, 32.3 ± 4, and 30.3 ± 5.8 nm, respectively. These evolutions plead in favor of the major importance of the surface roughness in promoting increases in both the Isc and the η. In our case, this can happen for the superior anatase content in the deposited structure, which could be the effect of the largest energy transfer. It could also be due to the different degrees of dye loading in the TiO_2 layer, if the differences in the thicknesses of the active TiO_2 layers in the cells are taken into account. One may therefore assume that, in addition to the superior conduction-band edge energy of the anatase [55,56], the surface quality is attributable to the prevalent role of this phase and the dye loading [5] as a function of the active layer thickness in increasing the short-circuit current and, finally, the photovoltaic conversion efficiency.

The reported results support, in our opinion, the key role of the roughness (RMS) in controlling the photovoltaic efficiency (η) value; i.e., the higher the roughness, the larger the photovoltaic conversion efficiency. This is particularly obvious when comparing the evolutions in the case of He versus Ar, which possess the highest η and RMS values, even though the thicknesses are about 24 times different between the two cases, which made them hardly detectable by the XRD that the film deposited in Ar.
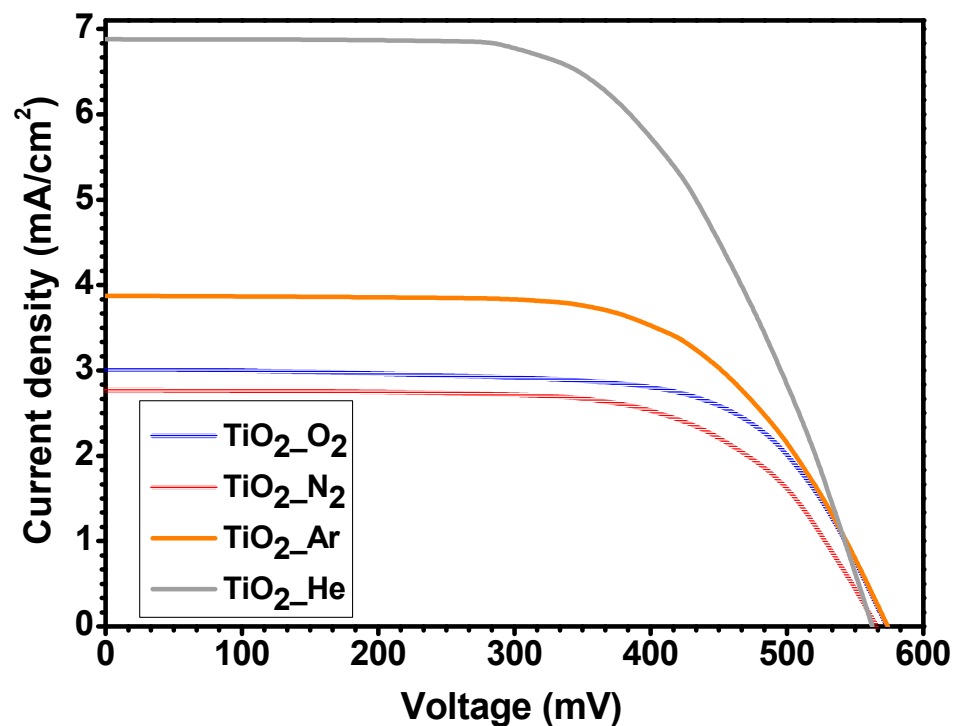
Figure 5. Current–voltage curves for typical dye-sensitized solar cells fabricated using photoelectrodes with various coatings: $TiO_2\_O_2$ (**blue line**); $TiO_2\_N_2$ (**red line**); TiO_2_Ar (**orange line**); and TiO_2_He (**grey line**). The measurements were carried out under standard AM 1.5G illumination conditions.

Table 3. Electro-optical parameters: short-circuit current (I_{SC}); open-circuit voltage (V_{OC}); short-circuit current density (J_{SC}); maximum power (P_{max}); fill factor (FF); and photovoltaic conversion efficiency (η) of typical DSSCs measured under standard illumination conditions.

Sample	*Isc* (mA)	*Voc* (mV)	*Jsc* (mA/cm^2)	*Pmax* (μW)	*FF*	η (%)
$TiO_2\_O_2$	2.37	573.4	3.014	930	0.69	1.18
$TiO_2\_N_2$	2.18	565.7	2.771	802	0.65	1.02
TiO_2_Ar	3.04	574.0	3.873	1117	0.64	1.42
TiO_2_He	5.40	562.7	6.881	1825	0.60	2.32

As is known, the photoanode stands for the key element in the DSSC cell configuration because its surface can retain a smaller/larger quantity of dye, which controls the absorption and, thus, the cell conversion efficiency. Therefore, the main aim of this work was to compare the PLD capabilities of depositing the same material (TiO_2) in very different ambient gases (as He, N_2, O_2, and Ar) to obtain various geometrical (pores) configurations in order to retain the largest possible quantity of dye.

Our results demonstrate that the best efficiency was reached under similar deposition conditions and the same poured dye loading by the films synthetized in the He atmosphere. This performance is supported by the SEM data, which indicates smaller but denser surface conglomerations in the case of ambient He, which, according to the current literature [57–59], facilitate the deeper and more efficient penetration of the fluid into the structure. This assertion is also supported by the results in [60,61].

4. Conclusions

We report on the preparation of new structures that are suitable for the manufacture of DSSCs with notable photovoltaic performance. For this purpose, the active semiconductor

layer of the TiO_2 in the anode structure of the solar cells was deposited via PLD with a KrF* excimer laser source, in various gas ambiences (O_2, N_2, Ar, or He). The deposited TiO_2 semiconductor structures with increased surfaces allowed for a better adsorption of the N719 (dye) photosensitizer.

The high-magnification SEM images evidence a uniform distribution of the TiO_2 nanograins, with well-defined boundaries. In the cases of the TiO_2_N_2 and TiO_2_Ar batches, compaction could be noticed, as compared to TiO_2_O_2 and TiO_2_He, which most likely resulted in a porosity decrease.

The decreasing trend in the film thickness was not only observed for a smaller number of applied pulses, but also for larger molecule sizes (from He, N_2, O_2, to Ar), and the pressure of the ambient gas. However, a certain saturation tendency was observed in the two cases. The second evolution is due to the increase in the number of collisions of the ablated substance with the larger gas atoms/molecules.

The topographies of the TiO_2 coatings, which were examined by AFM, supported the columnar growth of the coatings and the uniform distribution of the material. The structures deposited in the He are the thickest and exhibited the largest roughness.

The XRD patterns reveal that the TiO_2 coatings mainly consist of the anatase–rutile phases, both with tetragonal structures. A higher crystallinity was observed in the case of the TiO_2_He sample, while a lower crystallinity was observed for TiO_2_Ar.

The mentioned evolutions were reflected in the values of the electro-optical parameters, particularly those of the short-circuit current (*Isc*) and the photovoltaic conversion efficiency (η). The best performance was recorded for TiO_2_He, for which $Isc = 5.40$ mA and $\eta = 2.32\%$; i.e., its performance was about twice as superior to the TiO_2_O_2. On the other hand, the values of the filling factors (*FF*) are comparable (~ 0.6) for all the coatings.

These behaviors were found in accordance not only with the anatase content in the deposited structures, but also with the topographies (roughness) of the obtained surfaces. One may conclude that a significant increase in the electro-optical performances of the PV cells with anodes covered with TiO_2 layers deposited in the various gases can be expected via the optimization of the PLD deposition conditions so as to ensure an increase in both the *Isc* and the η.

The intention is to perform replications of the best samples (thick TiO_2 nanostructures) to fabricate DSSCs for use in common research/application work.

References

1. Grätzel, M. Photoelectrochemical cells. *Nature* **2001**, *414*, 338–344. [CrossRef] [PubMed]
2. Bahnemann, D. Photocatalytic water treatment: Solar energy applications. *Sol. Energy* **2004**, *77*, 445–459. [CrossRef]
3. Perera, F. Pollution from Fossil-Fuel Combustion is the Leading Environmental Threat to Global Pediatric Health and Equity: Solutions Exist. *Int. J. Environ. Res. Public Health* **2018**, *15*, 16. [CrossRef] [PubMed]
4. Chapin, D.M.; Fuller, C.S.; Pearson, G.L. A New Silicon p-n Junction Photocell for Converting Solar Radiation into Electrical Power. *J. Appl. Phys.* **1954**, *25*, 676–677. [CrossRef]
5. O'Regan, B.; Grätzel, M. A low-cost, high-efficiency solar cell based on dye-sensitized colloidal TiO$_2$ films. *Nature* **1991**, *353*, 737–740. [CrossRef]
6. Tong, Z.; Peng, T.; Sun, W.; Liu, W.; Guo, S.; Zhao, X.-Z. Introducing an Intermediate Band into Dye-Sensitized Solar Cells by W6+ Doping into TiO$_2$ Nanocrystalline Photoanodes. *J. Phys. Chem. C* **2014**, *118*, 16892–16895. [CrossRef]
7. Kakiage, K.; Aoyama, Y.; Yano, T.; Otsuka, T.; Kyomen, T.; Unno, M.; Hanaya, M. An achievement of over 12 percent efficiency in an organic dye-sensitized solar cell. *Chem. Commun.* **2014**, *50*, 6379–6381. [CrossRef]
8. Graetzel, M.; Janssen, R.A.J.; Mitzi, D.B.; Sargent, E.H. Materials interface engineering for solution-processed photovoltaics. *Nature* **2012**, *488*, 304–312. [CrossRef]
9. Mariotti, N.; Bonomo, M.; Fagiolari, L.; Barbero, N.; Gerbaldi, C.; Bella, F.; Barolo, C. Recent advances in eco-friendly and cost-effective materials towards sustainable dye-sensitized solar cells. *Green Chem.* **2020**, *22*, 7168–7218. [CrossRef]
10. Yeoh, M.-E.; Chan, K.-Y. Recent advances in photo-anode for dye-sensitized solar cells: A review. *Int. J. Energy Res.* **2017**, *41*, 2446–2467. [CrossRef]
11. Scarabino, S.; Nonomura, K.; Vlachopoulos, N.; Hagfeldt, A.; Wittstock, G. Effect of TiO$_2$ Photoanodes Morphology and Dye Structure on Dye-Regeneration Kinetics Investigated by Scanning Electrochemical Microscopy. *Electrochem* **2020**, *1*, 329–343. [CrossRef]
12. Toe, M.Z.; Matsuda, A.; Han, S.S.; Yaacob, K.A.; Pung, S.-Y. Effect of annealing temperature on the performance of ZnO thin film-based dye sensitized solar cell. *AIP Conf. Proc.* **2020**, *2267*, 20010. [CrossRef]
13. Dhamodharan, P.; Chen, J.; Manoharan, C. Fabrication of dye-sensitized solar cells with ZnO nanorods as photoanode and natural dye extract as sensitizer. *J. Mater. Sci. Mater. Electron.* **2021**, *32*, 13418–13429. [CrossRef]
14. Sufyan, M.; Mehmood, U.; Gill, Y.Q.; Nazar, R.; Khan, A.U.H. Hydrothermally synthesize zinc oxide (ZnO) nanorods as an effective photoanode material for third-generation Dye-sensitized solar cells (DSSCs). *Mater. Lett.* **2021**, *297*, 130017. [CrossRef]
15. Lee, T.-H.; Sue, H.-J.; Cheng, X. Solid-state dye-sensitized solar cells based on ZnO nanoparticle and nanorod array hybrid photoanodes. *Nanoscale Res. Lett.* **2011**, *6*, 517. [CrossRef] [PubMed]
16. Yildiz, Z.K.; Atilgan, A.; Atli, A.; Özel, K.; Altinkaya, C.; Yildiz, A. Enhancement of efficiency of natural and organic dye sensitized solar cells using thin film TiO$_2$ photoanodes fabricated by spin-coating. *J. Photochem. Photobiol. A Chem.* **2019**, *368*, 23–29. [CrossRef]
17. Gnida, P.; Jarka, P.; Chulkin, P.; Drygała, A.; Libera, M.; Tański, T.; Schab-Balcerzak, E. Impact of TiO$_2$ Nanostructures on Dye-Sensitized Solar Cells Performance. *Materials* **2021**, *14*, 1633. [CrossRef]
18. Kathirvel, S.; Chen, H.-S.; Su, C.; Wang, H.-H.; Li, C.-Y.; Li, W.-R. Preparation of Smooth Surface TiO$_2$ Photoanode for High Energy Conversion Efficiency in Dye-Sensitized Solar Cells. *J. Nanomater.* **2013**, *2013*, 367510. [CrossRef]
19. Tsai, J.K.; Hsu, W.D.; Wu, T.C.; Meen, T.H.; Chong, W.J. Effect of compressed TiO$_2$ nanoparticle thin film thickness on the performance of dye-sensitized solar cells. *Nanoscale Res. Lett.* **2013**, *8*, 459. [CrossRef]
20. Ahmad, M.S.; Pandey, A.K.; Rahim, N.A. Towards the plasmonic effect of Zn nanoparticles on TiO$_2$ monolayer photoanode for dye sensitized solar cell applications. *Mater. Lett.* **2017**, *195*, 62–65. [CrossRef]
21. Tyagi, J.; Gupta, H.; Purohit, L.P. Mesoporous ZnO/TiO$_2$ photoanodes for quantum dot sensitized solar cell. *Opt. Mater.* **2021**, *115*, 111014. [CrossRef]
22. Zhang, Q.; Li, C. TiO$_2$ Coated ZnO Nanorods by Mist Chemical Vapor Deposition for Application as Photoanodes for Dye-Sensitized Solar Cells. *Nanomaterials* **2019**, *9*, 1339. [CrossRef]
23. Bhogaita, M.; Devaprakasam, D. Hybrid photoanode of TiO$_2$-ZnO synthesized by co-precipitation route for dye-sensitized solar cell using phyllanthus reticulatas pigment sensitizer. *Sol. Energy* **2021**, *214*, 517–530. [CrossRef]
24. Kumi-Barimah, E.; Penhale-Jones, R.; Salimian, A.; Upadhyaya, H.; Hasnath, A.; Jose, G. Phase evolution, morphological, optical and electrical properties of femtosecond pulsed laser deposited TiO$_2$ thin films. *Sci. Rep.* **2020**, *10*, 10144. [CrossRef] [PubMed]
25. Deepa, H.A.; Madhu, G.M.; Venkatesham, V. Performance evaluation of DSSC's fabricated employing TiO$_2$ and TiO$_2$-ZnO nanocomposite as the photoanodes. *Mater. Today Proc.* **2021**, *46*, 4579–4586. [CrossRef]
26. Lungu, J.; Socol, G.; Stan, G.E.; Ştefan, N.; Luculescu, C.; Georgescu, A.; Popescu-Pelin, G.; Prodan, G.; Gîrţu, M.A.; Mihăilescu, I.N. Pulsed laser fabrication of TiO$_2$ buffer layers for dye sensitized solar cells. *Nanomaterials* **2019**, *9*, 746. [CrossRef]
27. Socol, G.; Gnatyuk, Y.; Stefan, N.; Smirnova, N.; Djokić, V.; Sutan, C.; Malinovschi, V.; Stanculescu, A.; Korduban, O.; Mihailescu, I.N. Photocatalytic activity of pulsed laser deposited TiO$_2$ thin films in N$_2$, O$_2$ and CH$_4$. *Thin Solid Films* **2010**, *518*, 4648–4653. [CrossRef]
28. Chrisey, D.B.; Hubler, G.K. *Pulsed Laser Deposition of Thin Films*; Wiley: Hoboken, NJ, USA, 1994; ISBN 9780471592181.
29. Eason, R. *Pulsed Laser Deposition of Thin Films: Applications-Led Growth of Functional Materials*; Wiley: Hoboken, NJ, USA, 2007; ISBN 9780470052112.

30. Fusi, M.; Maccallini, E.; Caruso, T.; Casari, C.S.; Li Bassi, A.; Bottani, C.E.; Rudolf, P.; Prince, K.C.; Agostino, R.G. Surface electronic and structural properties of nanostructured titanium oxide grown by pulsed laser deposition. *Surf. Sci.* **2011**, *605*, 333–340. [CrossRef]

31. Mihailescu, I.N.; Lita, A.; Teodorescu, V.S.; Luches, A.; Martino, M.; Perrone, A.; Gartner, M. Pulsed laser deposition of silicon nitride thin films by laser ablation of a Si target in low pressure ammonia. *J. Mater. Sci.* **1996**, *31*, 2839–2847. [CrossRef]

32. Gyorgy, E.; Mihailescu, I.N.; Κομπίτσας, M.; Giannoudakos, A. Particulates-free Ta thin films obtained by pulsed laser deposition: The role of a second laser in the laser-induced plasma heating. *Appl. Surf. Sci.* **2002**, *195*, 270–276. [CrossRef]

33. Amoruso, S. 6—Plume characterization in pulsed laser deposition of metal oxide thin films. In *Metal Oxides*; Pryds, N., Esposito, V., Korotcenkov, G., Eds.; Elsevier: Amsterdam, The Netherlands, 2018; pp. 133–160. ISBN 978-0-12-811166-6.

34. Yap, S.S.; Yong, T.K.; Nee, C.H.; Tou, T.Y. Pulsed Laser Deposition of ITO: From Films to Nanostructures. In *Applications of Laser Ablation—Thin Film Deposition, Nanomaterial Synthesis and Surface Modification*; Yong, T.K., Ed.; IntechOpen: Rijeka, Croatia, 2016; p. 4. ISBN 978-953-51-2812-0.

35. Dawood, M.S.; Hamdan, A.; Margot, J. Influence of surrounding gas, composition and pressure on plasma plume dynamics of nanosecond pulsed laser-induced aluminum plasmas. *AIP Adv.* **2015**, *5*, 107143. [CrossRef]

36. Hagfeldt, A.; Boschloo, G.; Sun, L.; Kloo, L.; Pettersson, H. Dye-Sensitized Solar Cells. *Chem. Rev.* **2010**, *110*, 6595–6663. [CrossRef] [PubMed]

37. Nazeeruddin, M.K.; Kay, A.; Rodicio, I.; Humphry-Baker, R.; Mueller, E.; Liska, P.; Vlachopoulos, N.; Graetzel, M. Conversion of light to electricity by cis-X2bis(2,2′-bipyridyl-4,4′-dicarboxylate)ruthenium(II) charge-transfer sensitizers (X = Cl⁻, Br⁻, I⁻, CN⁻, and SCN⁻) on nanocrystalline titanium dioxide electrodes. *J. Am. Chem. Soc.* **1993**, *115*, 6382–6390. [CrossRef]

38. Smestad, G.; Gratzel, M. Demonstrating Electron Transfer and Nanotechnology: A Natural Dye-Sensitized Nanocrystalline Energy Converter. *J. Chem. Educ.* **1998**, *75*, 75. [CrossRef]

39. Millington, K.R.; Fincher, K.W.; King, A.L. Mordant dyes as sensitisers in dye-sensitised solar cells. *Sol. Energy Mater. Sol. Cells* **2007**, *91*, 1618–1630. [CrossRef]

40. Georgescu, A.; Damache, G.; Gîtu, M.A. Class A small area solar simulator for dye-sensitized solar cell testing. *J. Optoelectron. Adv. Mater.* **2008**, *10*, 3003–3007.

41. Hafez, H.S.; Shenouda, S.S.; Fadel, M. Photovoltaic characteristics of natural light harvesting dye sensitized solar cells. *Spectrochim. Acta A Mol. Biomol. Spectrosc.* **2018**, *192*, 23–26. [CrossRef]

42. Wen, K.; Liu, M.; Liu, X.; Deng, C.; Zhou, K. Deposition of Photocatalytic TiO₂ Coating by Modifying the Solidification Pathway in Plasma Spraying. *Coatings* **2017**, *7*, 169. [CrossRef]

43. Iliescu, M.; Nelea, V.; Werckmann, J.; Mihailescu, I.N.; Socol, G.; Bigi, A.; Bracci, B. Electron microscopy studies of octa-calcium phosphate thin films obtained by pulsed laser deposition. *Thin Solid Films* **2004**, *453–454*, 157–161. [CrossRef]

44. Mihailescu, I.N.; Teodorescu, V.S.; Gyorgy, E.; Luches, A.; Perrone, A.; Martino, M. About the nature of particulates covering the surface of thin films obtained by reactive pulsed laser deposition. *J. Phys. D Appl. Phys.* **1998**, *31*, 2236–2240. [CrossRef]

45. Popescu, A.C.; Stan, G.E.; Duta, L.; Nita, C.; Popescu, C.; Surdu, V.-A.; Husanu, M.-A.; Bita, B.; Ghisleni, R.; Himcinschi, C.; et al. The Role of Ambient Gas and Pressure on the Structuring of Hard Diamond-Like Carbon Films Synthesized by Pulsed Laser Deposition. *Materials* **2015**, *8*, 3284–3305. [CrossRef]

46. Bergström, D.; Powell, J.; Kaplan, A.F.H. The absorption of light by rough metal surfaces—A three-dimensional ray-tracing analysis. *J. Appl. Phys.* **2008**, *103*, 103515. [CrossRef]

47. Bergström, D.; Powell, J.; Kaplan, A.F.H. A ray-tracing analysis of the absorption of light by smooth and rough metal surfaces. *J. Appl. Phys.* **2007**, *101*, 113504. [CrossRef]

48. Abedi, H.; Hoseinpour Gollo, M. An experimental study of the effects of surface roughness and coating of Cr2O3 layer on the laser-forming process. *Opt. Laser Technol.* **2019**, *109*, 336–347. [CrossRef]

49. Scholtz, L.; Ladanyi, L.; Mullerova, J. Influence of surface roughness on optical characteristics of multilayer solar cells. *Adv. Electr. Electron. Eng.* **2014**, *12*, 631–638. [CrossRef]

50. Ding, J.; Li, Y.; Hu, H.; Bai, L.; Zhang, S.; Yuan, N. The influence of anatase-rutile mixed phase and ZnO blocking layer on dye-sensitized solar cells based on TiO₂ nanofiber photoanodes. *Nanoscale Res. Lett.* **2013**, *8*, 9. [CrossRef]

51. Hao, Q.; Fu, X.; Song, S.; Gibson, D.; Li, C.; Chu, H.O.; Shi, Y. Investigation of TiO₂ Thin Film Deposited by Microwave Plasma Assisted Sputtering and Its Application in 3D Glasses. *Coatings* **2018**, *8*, 270. [CrossRef]

52. Ba-Abbad, M.; Kadhum, A.; Mohamad, A.B.; Takriff, M.; Sopian, K. Synthesis and Catalytic Activity of TiO₂ Nanoparticles for Photochemical Oxidation of Concentrated Chlorophenols under Direct Solar Radiation. *Int. J. Electrochem. Sci.* **2012**, *7*, 4871–4888.

53. Wiatrowski, A.; Mazur, M.; Obstarczyk, A.; Wojcieszak, D.; Kaczmarek, D.; Morgiel, J.; Gibson, D. Comparison of the Physico-chemical Properties of TiO₂ Thin Films Obtained by Magnetron Sputtering with Continuous and Pulsed Gas Flow. *Coatings* **2018**, *8*, 412. [CrossRef]

54. Khan, A.F.; Mehmood, M.; Durrani, S.K.; Ali, M.L.; Rahim, N.A. Structural and optoelectronic properties of nanostructured TiO₂ thin films with annealing. *Mater. Sci. Semicond. Process.* **2015**, *29*, 161–169. [CrossRef]

55. Wold, A. Photocatalytic Properties of TiO₂. *Chem. Mater.* **1993**, *5*, 280–283. [CrossRef]

56. Hoffmann, M.R.; Martin, S.T.; Choi, W.; Bahnemann, D.W. Environmental Applications of Semiconductor Photocatalysis. *Chem. Rev.* **1995**, *95*, 69–96. [CrossRef]

57. Sima, F.; Sugioka, K. Ultrafast laser manufacturing of nanofluidic systems. *Nanophotonics* **2021**, *10*, 2389–2406. [CrossRef]

58. Bocquet, L. Nanofluidics coming of age. *Nat. Mater.* **2020**, *19*, 254–256. [CrossRef]
59. Bocquet, L.; Charlaix, E. Nanofluidics, from bulk to interfaces. *Chem. Soc. Rev.* **2010**, *39*, 1073–1095. [CrossRef]
60. Islam, S.Z.; Reed, A.; Kim, D.Y.; Rankin, S.E. N_2/Ar plasma induced doping of ordered mesoporous TiO_2 thin films for visible light active photocatalysis. *Microporous Mesoporous Mater.* **2016**, *220*, 120–128. [CrossRef]
61. Yao, Z.; Jia, F.; Tian, S.; Li, C.; Jiang, Z.; Bai, X. Microporous Ni-Doped TiO_2 film Photocatalyst by Plasma Electrolytic Oxidation. *ACS Appl. Mater. Interfaces* **2010**, *2*, 2617–2622. [CrossRef]